RESEARCH ARTICLE

Effects of Turbulence Parameterization on Hydrodynamics and Sediment Transport in Tidal Channels: A Case Study of Yamen Channel in the Northern South China Sea

Yi Yang[1], Jingui Liu[2], Yichun Li[3] and Chunhua Zhang[1]

Abstract

In this study, we conducted numerical experiments to examine the effects of turbulence parameterization on temporal and spatial variations of suspended sediment dynamics. Then, we applied the numerical model to the Yamen Channel, one of the main eight outfalls in the Pearl River Delta. For the field application, we implemented the $k-\varepsilon$ scheme with a reasonable stability function using the continuous deposition formula during the erosion process near the water-sediment interface. We further validated and analyzed the temporal-spatial suspended sediment concentrations (SSCs). The experimental results show that under specified initial and boundary conditions, turbulence parameterization with stability functions can lead to different vertical profiles of the velocity and SSC. The $k-\varepsilon$ predicts stronger mixing with a maximum value of approximately twice the $k-kl$. The $k-kl$ results in smaller SSCs near the surface layer and a larger vertical gradient than the $k-\varepsilon$. In the Yamen Channel, though the turbulent dissipation, turbulent viscosity and turbulence kinetic energy exhibit similar trends, SSCs differ significantly between those at low water and high water due to the tidal asymmetry and settling lag mechanisms. The results can provide significant insights into environmental protection and estuarine management in the Pearl River Delta.

Keywords Suspended sediment; General ocean turbulence model (GOTM); Turbulence parameterization; Yamen Channel; Finite volume community ocean model (FVCOM)

Article Highlights

• Numerical experiments were conducted to examine the effects of turbulence parameterization on suspended sediment dynamics.
• The $k-\varepsilon$ scheme predicts stronger mixing with a maximum value of approximately twice the $k-\varepsilon$. The $k-\varepsilon$ results in smaller SSCs near the surface layer and a larger vertical gradient than the $k-\varepsilon$.
• Suspended sediment concentrations (SSCs) differ significantly between those at low water and high water due to the tidal asymmetry and settling lag mechanisms in the Yamen Channel.

✉ Yichun Li
　ychlee@163.com

1　Haikou Marine Environment Monitoring Station, State Oceanic Administration, Haikou 570000, China

2　College of Ocean and Meteorology, Guangdong Ocean University, Zhanjiang 524088, China

3　Key Laboratory of Harbour, Coastal and Offshore Engineering, Beibu Gulf University, Qinzhou 535011, China

1 Introduction

Turbulence parameterization is highly uncertain in both physical and sediment numerical models (Geyer and Ralston, 2015). In the past decades, the major focus on turbulence modelling is to suggest equations closures at various sophistication levels. Numerous modifications to these models have been proposed (Rodi, 1984; Chen and Beardsley, 1998; Umlauf et al., 2003; Burchard et al., 2014; Liu et al., 2022).

The $k-kl$ turbulence closure scheme (Mellor and Yamada level-2.5, MY2.5, MY1982) has been used widely in estuaries and coastal oceans. In the MY2.5, the vertical turbulent viscosity is calculated by solving the turbulence kinetic energy (TKE) equation and turbulence length scale equation. This scheme seems to work well for tidal-induced mixing in shallow waters (Chen and Beardsley, 1998), but further validation is needed for the estuarine regions. Several studies have been carried out to improve this turbulent model (Galperin et al., 1988; Burchard et al.,

1998; Burchard and Bolding, 2001). A modification of the macroscale equation has been introduced, together with a new wall proximity function to investigate the vertical structure of open channel flows (Blumberg et al., 1992). Rodi (1984) significantly advanced the $k-\varepsilon$. Recent contributions paid particular attention to the buoyancy parameterization and model comparison (Burchard et al., 1998; Burchard and Bolding, 2001; Burchard et al., 2014). Umlauf et al. (2003) suggested a generalization of a class of differential length-scale equations typically used in second-order turbulence models for oceanic flows. Generally used models, such as the $k-\varepsilon$ and the MY2.5, can be treated as special cases of this generic model. Recently, some studies have investigated physical and numerical turbulent-mixing behavior through numerical experiments (Reffray et al., 2015; Ralston et al., 2017; Costa et al., 2017; Tu et al., 2019; Choi et al., 2021).

Since vertical diffusion is one of the key processes for suspended sediment concentration (SSC) in estuaries, the uncertainty due to various turbulence parameterization schemes should be considered in the assessment of the reliability of the sediment transport model. Warner et al. (2005) evaluated the performance of four turbulence closure models and their influences on suspended sediment transport using a generic length scale method with several ideal cases based on ROMS. In this contribution, we carry out numerical experiments to investigate the impacts of turbulence parameterization on the suspended-sediment profile, together with different stability functions. We conducted the experiments by running FVCOM with various turbulence closure modules implemented in the General Ocean Turbulence Model (GOTM).

In recent years, since the reclamation on both sides of the waterway and the evolution of shoals, the deposition in local thalweg areas has aggravated to obstruct navigation (Lima et al., 2021; Wu et al., 2022). Yang and Wang (1994), and Chen et al. (2003) have conducted numerical simulations of the tidal wave and sediment transport in the Pearl River, but without systematic analyses in the Yamen Channel, which is one of the eight outfalls of the Pearl River. It is of great significance to investigate the hydrodynamics and suspended sediment transport in this area. Recently, some studies have been carried out in the Pearl River estuary (Zhang et al., 2019; Yang et al., 2022). To further investigate the turbulence simulation and better understand its impact on the sediment dynamics in the Pearl River Estuary, we conduct numerical simulations to investigate the sensitivity of turbulence parameterization on vertical distributions of velocity and SSC in the Yamen Channel. This paper is structured as follows: after describing the study area and observations (Section 2), we present three main modules of the numerical model together with model configuration (Section 3). Section 4 gives the sensitivity analysis of turbulence parameterization and model validation, followed by a detailed investigation of the spatial-temporal variations of SSC and intra-tidal variations of turbulent parameters, vertical velocity, and SSC. The conclusions are listed in Section 5.

2 Study area and observations

Yamen Channel, located at the head of the Huangmao Sea (HM Sea), is the westernmost one of the eight outfalls (YM: Yamen, HTM: Hutiaomen, JTM: Jitimen, MDM: Modaomen, HM: Hengmen, HQM: Hongqimen, JM: Jiaomen, HuM: Humen) of the Pearl River Delta (Figure 1). In Figure 1, Z2, Z3 and Z4 are sites for water levels. A3, A4, and A5 are for velocity and SSCs. The runoff of the Tanjiang River (TR) flows into HM Sea through the Yamen Channel. This typical tidal-dominated channel is an important navigable waterway, which is surrounded by extensive intertidal salt marshes and numerous tidal creeks. The annual discharge is about 196×10^8 m³, which covers 6% of the total runoff of the Pearl River (Figure 1). Compared to the strong tidal current, the river flow appears weak. The average tidal range is approximately 1.24 m. The model domain is up to the Tanjiang River, and reaches the HM Sea downstream. A comparison between the Yamen and the Hutiaomen (HTM) at the HM Sea is shown in Table 1.

The medium diameter of the suspended load is less than 0.1 mm and the diameter of sediment particles from the upstream during ebb tide is larger than that from the outer sea during flood tide. In flood season, flow with high SSC enters the Yamen channel. The mean grain size is about 5 μm. The sediment is mainly transported in suspension. The particle diameter of bed sediment between 0.005−0.05 mm covers about 50%, and the median particle size is less than 0.05 mm.

3 Numerical Model

3.1 Hydrodynamic model

We adopted an unstructured-grid, three-dimensional primitive equation community ocean model FVCOM (Finite Volume Community Ocean Model) in this study (Chen et al., 2007). It solves the governing equations in unstructured triangular mesh by finite-volume method, which provides accurate conservations of mass, momentum, heat, and salt. This model has been applied to a number of estuaries and coastal oceans characterized by highly irregular geometry, large intertidal salt marshes, and steeply sloping bottom topography (Ding et al., 2013; Lai et al., 2015; Sun et al., 2016).
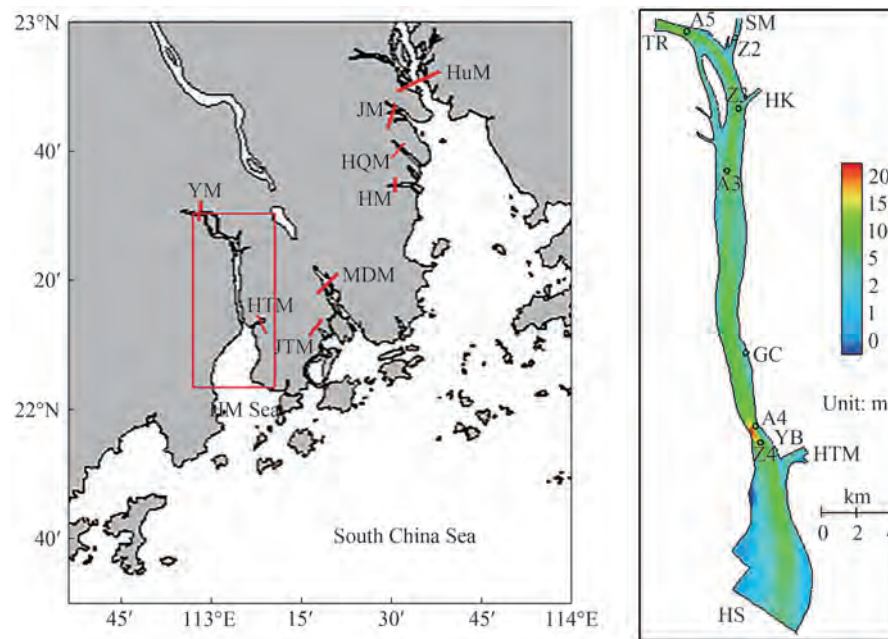
Figure 1 The sketch and the local topography of the Yamen channel (the red rectangle, TR: Tanjiang River, HS: HuShan, YB: Yamen Bridge, GC: GuanChong, HK: Hukeng, SM: Sanjiang Mouth.)

Table 1 Comparison between the water-sediment distribution and tidal range between YM and HTM at the HM Sea

Items	Branches		
	HTM	YM	Total amount of 8 branches
Annual discharge (10^8 m^3)	202.0	196.0	3 260.0
Percent (%) (the discharge of the Pearl River)	6.2	6.0	100.0
Annual sediment transport rate (10^4 t)	509.0	363.0	8 872.0
Percent (%) (the sediment of the Pearl River)	7.2	5.1	100.0
Annual-averaged tidal range (m)	1.20	1.24	
The maximum tidal range	2.66	2.95	
Annual flood tide volume (10^8 m^3)	57.0	636.0	3 763.0
The ratio of total runoff and flood tide volume	3.54	0.31	

3.2 Suspended sediment model

Suspended sediment is simulated by the three-dimensional suspended sediment equation in σ-coordinate:

$$\frac{\partial C}{\partial t} + \frac{\partial uC}{\partial x} + \frac{\partial vC}{\partial y} + \frac{1}{H}\frac{\partial wC}{\partial \sigma} = \frac{\partial}{\partial x}\left(A_h\frac{\partial C}{\partial x}\right) +$$
$$\frac{\partial}{\partial y}\left(A_h\frac{\partial C}{\partial y}\right) + \frac{1}{H}\frac{\partial}{\partial \sigma}\left(\frac{K_h}{H}\frac{\partial C}{\partial \sigma}\right) + \frac{1}{H}\frac{\partial C\omega_s}{\partial \sigma} \quad (1)$$

where A_h is the horizontal diffusion coefficient, K_h is the vertical diffusion coefficient, C is the suspended sediment concentration, ω_s is the settling velocity, H is total water depth, and (u, v, w) represent horizontal and vertical velocity, respectively.

Sediment particles near the bed can be re-suspended when the bottom bed stress exceeds critical stress. The bottom boundary condition is determined by near-bed sediment flux (van Rijn, 2005; Li et al., 2008):

$$F_s = E - D \quad (2)$$

where F_s is near-bed sediment flux, E is erosion flux, and D is deposition flux. The deposition rate (D in kg/(m^{2}s)) is determined as the mass that is removed from the suspended load and integrated into the bed. It depends on the particle's sinking velocity ω_s, and the near bottom concentration C_b in kg/m^3:

$$D = \omega_s C_b \quad (3)$$

Erosion is an instantaneous process that is initiated when the bed shear stress exceeds a critical value τ_{ce}, which

is derived from the critical Shields parameter (Warner et al., 2008).

$$E = \begin{cases} Q\left(1 - P_b\right)F_b\left(\dfrac{\tau_b}{\tau_{ce}} - 1\right) & \text{if } \tau_b > \tau_{ce} \\[2ex] 0 & \text{if } \tau_b \leq \tau_{ce} \end{cases} \quad (4)$$

where Q is the erosion flux, P_b is the bottom porosity, F_b is the fraction of sediment and τ_{ce} represents critical shear stress.

In terms of the initial conditions, the suspended sediment concentration is zero for the normal component on the fixed boundary. At the outflow open boundary, it is determined as $\dfrac{\partial C}{\partial t} + v_n\dfrac{\partial C}{\partial n} = 0$, v_n is the normal velocity component, and n is the normal direction to the open boundary. For the inflow, $C = C_0$, where C_0 is the given values.

The sediment bed is represented by 3-D arrays with a user-specified, constant number of layers beneath each horizontal model cell. At the beginning of each time step, active-layer thickness z_a is calculated based on the relation (Warner et al., 2005, W2005)

$$z_a = \max\left[k_1\left(\tau_b - \tau_{ce}\right)\rho_0, 0\right] + k_2 D_{50} \quad (5)$$

where τ_b is bottom stress, τ_{ce} is the critical stress for erosion, D_{50} is the median particle size, and k_1 and k_2 are empirical coefficients (0.007 and 6.0, respectively). The thickness of the top bed layer has a minimum thickness equivalent to z_a.

3.3 Turbulent closure

The Reynolds stress tensor and the turbulent tracer flux need to be parameterized to close the hydrostatic primitive equations that resulted from the Reynolds-averaging Navier-Stokes equations. The transport equations are parameterized by approximations of the third-order moments and pressure correlation terms. Additional scaling and boundary layer assumptions further reduce the set of equations of the Reynolds stresses and turbulent scalar fluxes in the form as follows:

$$\overline{u'w'} = -K_M\frac{\partial U}{\partial z}, \ \overline{v'w'} = -K_M\frac{\partial V}{\partial z}, \ \overline{w'\rho'} = -K_H\frac{\partial \rho}{\partial z} \quad (6)$$

with

$$K_M = c\sqrt{2k}\, lS_M + v, \ K_H = c\sqrt{2k}\, lS_H + v_\theta \quad (7)$$

where ρ is total density, and U and V are velocity of the mean components in the horizontal directions, respectively. u', v', and w' are the turbulent components of velocity in the horizontal and vertical directions, respectively. K_M is

the turbulent viscosity, K_H is the turbulent diffusivity, and S_M and S_H are stability functions that describe the effects of shear and stratification, respectively. v and v_θ represent molecular viscosity and diffusivity, respectively. l is turbulent length scale.

The GOTM developed by Umlauf and Burchard (2003) is a community turbulence module and is continuously upgraded (Burchard et al., 2008; Reissmann et al., 2009; Umlauf and Burchard, 2011). This module includes two typical turbulence closure models, (1) $k–kl$ equation and (2) $k–\varepsilon$ equation. Both turbulence module groups include the original code with a Richardson number cut off between 0.2 and 1.0. The GOTM has been coupled to FVCOM through an interface library, thus one can select different turbulence schemes to replace the default setup of the MY2.5 turbulence closure scheme.

The turbulent closure schemes rely on the stability functions parameterizing the pressure-strain correlation terms of the Reynolds stress (Burchard and Bolding, 2001). Each stability function considers a different approximate equilibrium of the five pressure-strain effects, including isotropy, shear production, buoyancy production, non-isotropic contribution and vorticity contribution. Five different stability functions have been explored: the modified MY2.5 which only contains isotropy and shear productions (Galperin et al., 1988), KC (Kantha and Clayson, 1994) which includes both isotropic and non-isotropic contributions; BB which contains the isotropy shear and buoyancy turbulence productions (Burchard and Baumert, 1995); CA (Canuto et al, 2001) which includes all five pressure-strain terms; and CB (Burchard and Baumert, 1995; Canuto et al., 2001) which was deduced for an equilibrium state that turbulence dissipation balances turbulence productions. We implemented the original MY2.5, modified MY2.5 (G1988), and the KC stability functions in the $k–kl$ equation and the other three stability functions (BB, CA, and CB) for the $k–\varepsilon$ equation model (Table 2).

3.4 Model configuration

The model area is discretized by non-overlapping triangular cells with a horizontal resolution of 20−80 m. Twenty even sigma layers are separated in the vertical direction, which allows for a slightly smooth representation of finite-amplitude irregular bottom bathymetry. The total numbers of triangular elements and nodes are 6 295 and 3 563, respectively. The time step for the external mode is 0.1 s.

The model is forced by river flow at the upstream riverine boundary and by water level at the southern open boundary. Tanjiang River, Sanjiang Mouth, HuKeng, and HTM channel are all input sources of riverine discharges and SSCs. Hushan is the downstream control boundary with water level extracted from the tidal dataset TPXO7.2 (Egbert and Erofeeva, 2002). Topography is based on the nautical maps published Dec. 2004 as the model terrain

(Figure 1).

The wind is weak during the simulation period, thus wind-induced wave effects and wind forcing are not included in these simulations. We chose the Smagorinsky turbulence parameterization method for the horizontal diffusion coefficient.

Since the SSCs are relatively small (0.02−0.4 kg/m^3) along the channel, and the influence of turbid water on particle settling is neglected, the settling velocity is set as a constant of 0.75 mm/s for simplicity. The critical erosion shear stress is set to 0.04~0.06 N/m^2, and a mean value of 0.05 N/m^2 is used in the simulations. The erosion constant is 5×10^{-5} kg/(m^2 s) (Table 3).

4 Results and analysis

4.1 The sensitivity analysis of turbulence closures

We conducted sensitivity analysis based on turbulent closure methods using the $k − \varepsilon$ equations with stability functions of CA, CB, and BB, $k − kl$ with KC, MY2.5, and G1988, and Analysis (ANA). The ANA is an algebraic expression for the turbulent viscosity as $K_M = ku_*z(1 − z/H)$, where k is a coefficient, u_*, frictional velocity, z, distance above the sea bed, and H, total water depth. Z4 is located near the Yamen Bridge with a depth of ~10 m. We chose this site to investigate the influence of turbulence closure schemes on the vertical distributions of velocity and SSC.

4.1.1 Vertical profile of turbulent variables

As a measure of turbulence intensity, TKE is one of the most important variables related to the momentum transport through the bottom boundary layer (BBL). Figure 2a shows that the $k − kl$ with the three stability functions of KC, MY2.5, and G1988 generates almost identical patterns. The $k − \varepsilon$ produces a notable difference among the three different stability functions, especially in the lower half of water depth. The values of CB and BB are ~2 times larger than that of CA. ANA would become more turbulent than the other methods.

Turbulent dissipations computed by different stability functions keep in good consistency, except that ANA would dissipate strongly near the BBL (Figure 2b). Generally, ANA would overestimate both TKE and turbulent dissipation especially near the BBL.

The $k − kl$ generally underestimates turbulent viscosity by ~40% compared to that of $k − \varepsilon$ and ANA (Figure 2c). The maximum values of $k − \varepsilon$ and ANA are almost identical. The profile of turbulent viscosity demonstrates asymmetrical characteristics for all turbulent schemes. However, ANA and $k − kl$ show an asymmetry biased towards the lower layer of water depth, whereas $k − \varepsilon$ simulates an asymmetry towards the upper layer.

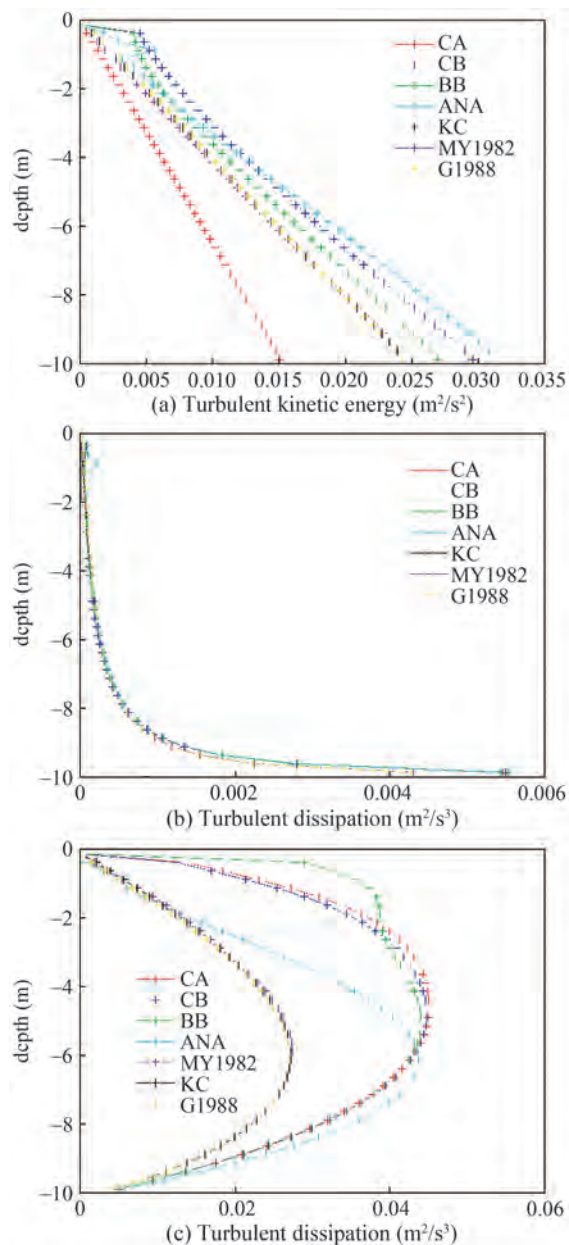#### 4.1.2 Vertical profiles of velocity and SSC

The vertical velocity profile shows two typical different patterns, especially in the surface layer (Figure 3a). The $k − kl$ with the three different stability functions and ANA produce anomalously high surface currents. This behavior has been documented (Blumberg et al., 1992; Burchard et al., 1998; Burchard and Bolding, 2001; Warner et al., 2005). Simulations by Warner et al. (2005) in open channel show that the original MY2.5 and $k − kl$ with parabolic wall function have abnormally high surface currents. This is consistent with the results of other turbulence schemes, including $k − \varepsilon$, $k − \omega$, ANA, and $k − kl$ with improved open channel wall function (Warner et al., 2005). In this paper, $k − \varepsilon$ schemes (CB, CA, BB) produce results that agree closely, while the surface flow velocities obtained using the $k − kl$ schemes including G1988, original MY2.5, KC, and ANA are excessively large. Warner et al. (2005) pointed out that the wrong wall function produces an incorrect mixing length scale, which leads to the underestimation of turbulent visibility far from the boundary. More-

Table 2 Turbulence parametrization including the stability functions

Turbulent scheme	Stability functions	Parameterizations				
		Isotropy	Shear production	Buoyancy Production	Non-isotropic	Vorticity
	BB	√		√		
$k − \varepsilon$	CA	√	√	√	√	√
	CB	Deduced by the quadrivium of turbulent dissipation and production.				
	MY2.5	Functions of the gradient Richardson number.				
$k − kl$	G1988	√	√			
	KC	√			√	

Table 3 Parameters of the hydrodynamic and sediment model

Horizontal resolution (m)	Nodes	Cells	Time step (s)	Settling velocity (mm/s)	τ_{ce} (N/m^2)	Erosion constant (kg/m^{2}s)
20-80	3 563	6 295	0.1	0.75	0.05	5×10^{-5}

Figure 2   Vertical distribution of turbulent parameters

tion and the open channel wall function, were introduced into the $k - kl$ scheme. The results show that the former made no improvement, but the open channel function eliminated the abnormally high surface current and produced results similar to those by $k - \varepsilon$, $k - \omega$, etc. (Warner et al., 2005). In this paper, we implemented three stable functions in the $k - kl$ and $k - \varepsilon$. The results show that an abnormally high surface current remains without introducing the correct wall function regardless of the stability functions.
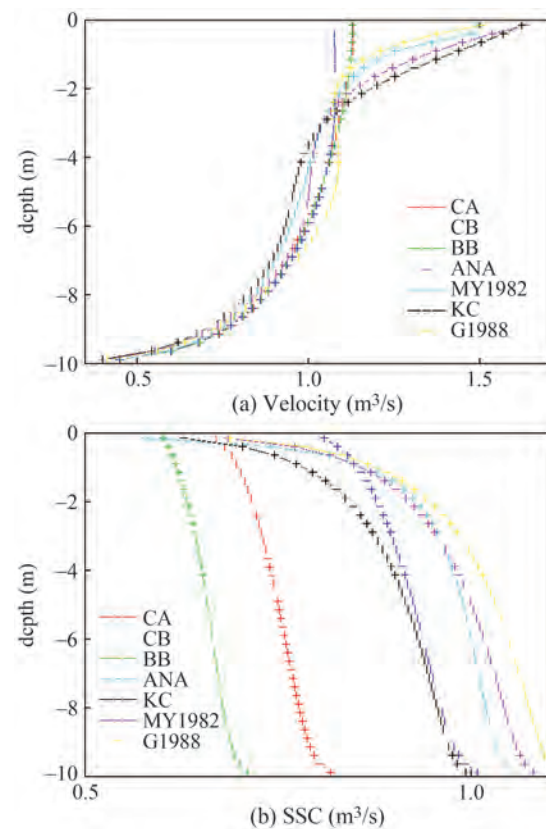
Figure 3   Vertical distribution of vertical velocity and SSC

over, other important consequences, besides the resultant higher depth-averaged velocities in the open channel, would also exist in the estuary. For instance, the mixing of fresh water and saline water in the estuary has a critical impact on the estuarine gravitational circulation (Hansen and Rattray, 1965). The gravitational circulation is suppressed when the vertical mixing is strong, and vice versa. Moreover, when surface velocity in the estuary is enhanced artificially, more water flux flows seaward in the upper layer. Due to the continuity, additional seawater should enter the estuary in the lower layer. This process will not only falsely enhance the estuarine circulation, but also affect the exchange capacity and time scale of material transport. In W2005, two wall functions, i.e., the parabolic wall func-

Different stability functions impose distinct influences on the vertical distribution of SSCs (Figure 3b). The $k - \varepsilon$ appears less gradient in the vertical direction than $k - kl$ near the upper layer (0−5 m). Suspended sediment distributes more uniformly in the vertical due to a larger diffusivity coefficient and an asymmetry towards the upper layer. Simulations by $k - \varepsilon$ may lead to wide variations in the magnitude of vertical-averaged SSCs. In W2005, ANA and $k - \omega$ generated the largest SSC. The $k - kl$ with parabolic wall function and the original MY2.5 produce the lowest values. The $k - \varepsilon$ and $k - kl$ with open channel wall functions are in between. Nevertheless, their vertical distributions of SSC display extremely similar patterns. In our simulations for the Yamen Channel, SSC based on ANA and $k - kl$ schemes are relatively large. Results by KC and CB are very close except obvious decrease by KC due to

the small turbulent diffusion in the surface layer. The results by CA and BB are smaller. This might be attributed to the relatively large turbulent viscosities of the CA and BB, which weakens the estuarine circulation and reduces upstream sediment transport.

Generally, the $k - kl$ closure scheme depends on wall function, which should be chosen with caution. Several alternate wall functions are proposed to produce an apparently correct parabolic turbulent viscosity profile. Given certain boundary and initial conditions, $k - \varepsilon$ produces more intensive vertical mixing than $k - kl$. On the other hand, the $k - kl$ tends to generate stratification. According to the vertical profile of turbulent parameters, vertical velocity, and SSCs, the CB function based on $k - \varepsilon$ generates reasonable patterns. Thus, we apply this parameterization to the model validation and further analysis in the Yamen Channel.

4.2 Model validation in the Yamen Channel

Based on the above sensitivity analysis, the $k - \varepsilon$ with CB stability function is chosen to validate the simulated results. Three metrics are used to quantify the agreements between observed and modeled data of water level, velocity, and SSC. A skill that has been widely used is written as (Willmott, 1981; Li et al., 2005):

$$\text{Skill} = 1 - \frac{\sum_{i=0}^{n} \left| x_{oi} - x_{mi} \right|^2}{\sum_{i=0}^{n} \left(\left| x_{oi} - \overline{x_o} \right| + \left| x_{mi} - \overline{x_o} \right| \right)^2} \quad (8)$$

where the subscript 'o' and 'm' indicate observed and modeled data respectively, and 'n' is the number of total time series. Another index to evaluate the absolute deviation of velocity and suspended sediment is mean absolute error (MAE):

$$\text{MAE} = \frac{\sum \left| x_{oi} - x_{mi} \right|}{n} \quad (9)$$

The deviation of the current direction is computed using mean absolute error coefficient (MAEC) defined in equation (10). Compared to equation (9), equation (10) emphasizes the contributions in the main directions and weakens the influences that arise from the slow slack flow which might be measured less precisely. The weights are chosen as square velocity amplitudes in the sense of kinetic energy.

$$\text{MAEC} = \frac{\sum_{i=0}^{n} \left(x_{oi} - x_{mi} \right) u_i^2}{\sum_{i=0}^{n} u_i^2} \quad (10)$$

where u is the velocity, and others are the same as the above.

We validated the modeled results against the observations during April 11−12 in 2005 (Figure 4). Though the

discrepancy increases slightly toward the downstream, the predictions show good agreement with the observations. We collected the statistics of water elevation with two metrics, MAE and Skill (Table 4). Skills are 0.99, and MAEs are less than 0.08 m at the three stations.
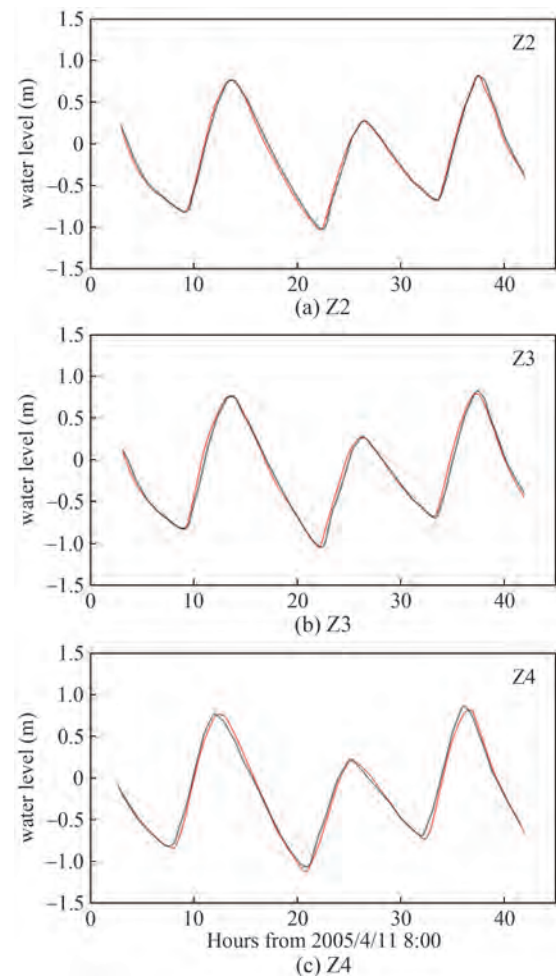
Figure 4   Validation of water elevation (black line for the modeled, red line for the observed)

Table 4   Statistics of water elevation

	Z2	Z3	Z4
MAE	0.021	0.033	0.085
Skill	0.99	0.99	0.99

The comparisons between the modeled and observed velocities at the three stations are shown in Table 5. MAEs of the velocity are 0.03−0.09 m/s. As the modeled and observed data are not at the exactly same location, and combined with grid resolution, some large deviations emerge. However, the Skills show good performance. MAECs of current direction are less than 11°, and Skills are larger than 0.9.

The comparisons of SSCs between the measured and predicted are shown in Figure 6 during the spring tide. Cir-

Table 5 Statistics of tidal velocity (m/s) and SSC (kg/m³)

		A3		A4		A5	
		0.2 h	0.8 h	0.2 h	0.8 h	0.2 h	0.8 h
Velocity	MAE	0.072	0.064	0.092	0.054	0.035	0.067
	Skill	0.97	0.97	0.93	0.98	0.99	0.98
SSC	MAE	0.018	0.048	0.045	0.07	0.016	0.039
	Skill	0.91	0.84	0.68	0.63	0.79	0.85

Table 6 Statistics of vertical average flow direction

	A3	A4	A5
MAEC	10.3	9.4	8.6
Skill	0.93	0.96	0.99

cle ("○") represents the measured and the thin line ("—") is the computed. The SSCs are lower than 0.4 kg/m³; in contrast, MAEs are less than 0.07 kg/m³. We concluded that the trend of SSC is considerably identical. According to the comparisons, the simulations are acceptable.
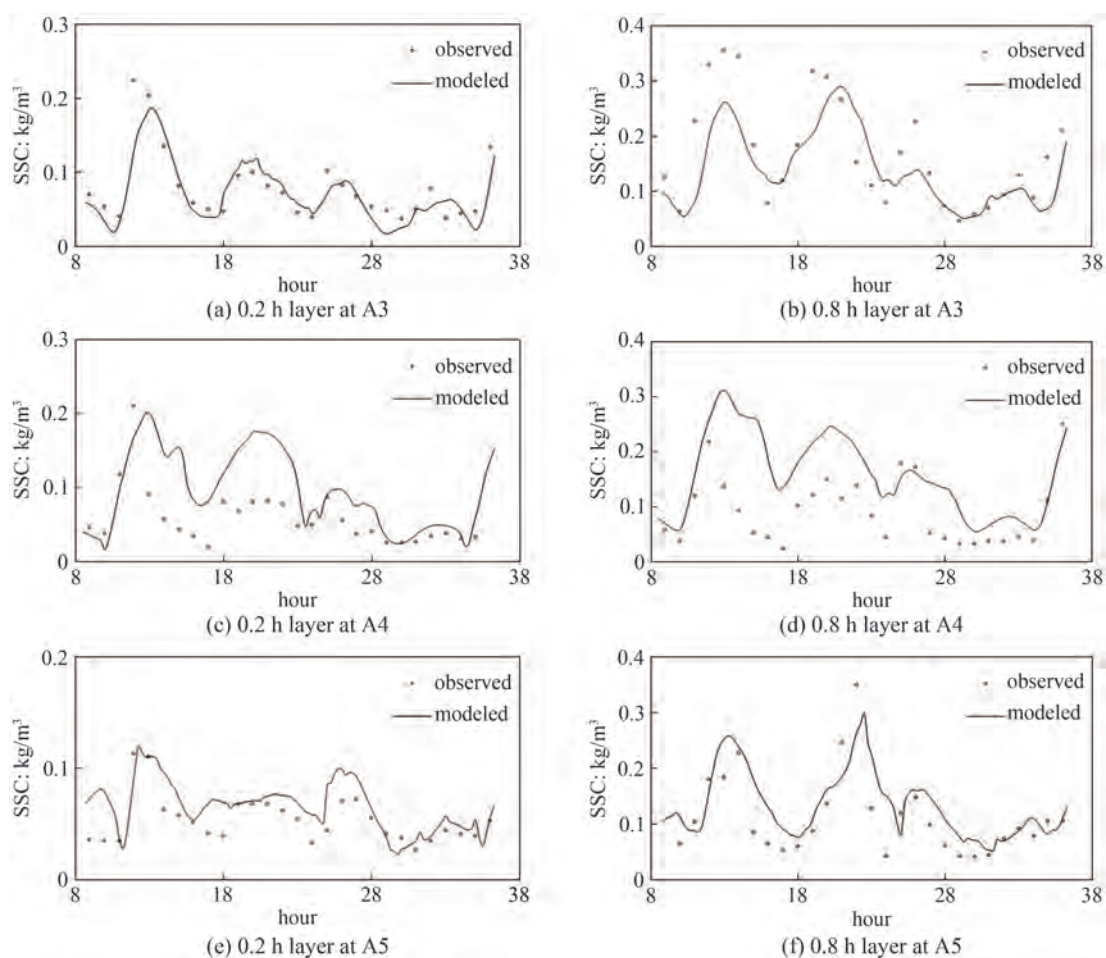
4.3 Spatial variations of SSC

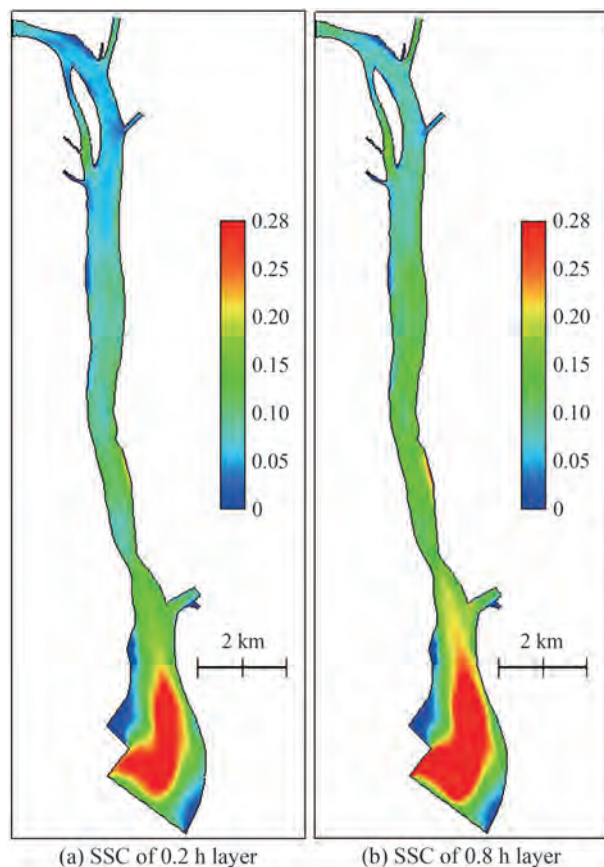The SSC fields of 0.2 h and 0.8 h layers during the

flood and ebb tide are presented in Figures 6 and 7, respectively. The SSCs to the south of Yamen Bridge are higher than that to the north during the flood tide, which vary from 0.1 to 0.3 kg/m³ and are basically lower than 0.1 kg/m³ to the north of the YB.

The SSCs of each layer during the flood tide are higher than that during the ebb tide, which can be attributed to the tidal asymmetry in the HM Sea. The mean duration of the ebb tide is longer than that of the flood tide, and tidal currents adversely. In the dry season, the duration of the ebb tide is longer than that of the flood tide for 1−2 hours. The bidirectional current flows mainly along the deep channel. Due to the tidal asymmetry in the channel, the flow velocity is smaller during the ebb tide than during the flood tide. Therefore, suspended particles tend to settle and deposit to the bed, and fewer sediment particles on the bed can be resuspended correspondingly.

The SSCs near the estuarine bar from the HTM to the middle channel are relatively high. At the same station, SSCs during the flood tide are higher than that during the ebb tide. The SSCs vary from 0.03 kg/m³ to 0.14 kg/m³ in the HM Sea. Due to the complicated interactions between the freshwater and shelf saline water and the effect of local ter-

**Figure 5** Comparisons of SSCs during the spring tide

(a) 0.2 h layer at A3
(b) 0.8 h layer at A3
(c) 0.2 h layer at A4
(d) 0.8 h layer at A4
(e) 0.2 h layer at A5
(f) 0.8 h layer at A5

(a) SSC of 0.2 h layer   (b) SSC of 0.8 h layer

Figure 6   SSC during flood maximum (kg/m^3)

rain, the SSCs exhibit obvious variations in the vertical.

4.4 Intratidal variations

According to the above analysis, we chose the results based on $k - \varepsilon$ and CB stability function to investigate the temporal variations of turbulent viscosity, turbulent kinetic energy, dissipation, velocity and SSC at site A3, which is located near the thalweg of the upstream channel in the Yamen Channel. The tidal currents exhibit a typical flood-dominated asymmetry. At high and low water, the velocity is extremely weak (Figure 8a). Flood current is larger than the ebb current of ~0.2 m/s, which is referred to the tidal velocity asymmetry (Song et al., 2011; Gong et al., 2016). The turbulent viscosity is extremely small at both high and low tide levels due to slack water. On the contrary, it is much greater at the maximum ebb and flood tide, which shows a positive correlation between turbulent viscosity and tidal velocity. The turbulent kinetic energy also shows similar variations. However, there is no obvious trend of dissipation. In W2005, the dissipations based on different schemes are nearly identical except MY2.5. Contrastingly, the results of turbulent kinetic energy are different. Moreover, the comparisons in W2005 are only at a timing of maximum ebb. Nonetheless, the simulated SSCs are considerably consistent except for that by MY2.5. This issue


(a) SSC of 0.2 h layer   (b) SSC of 0.8 h layer
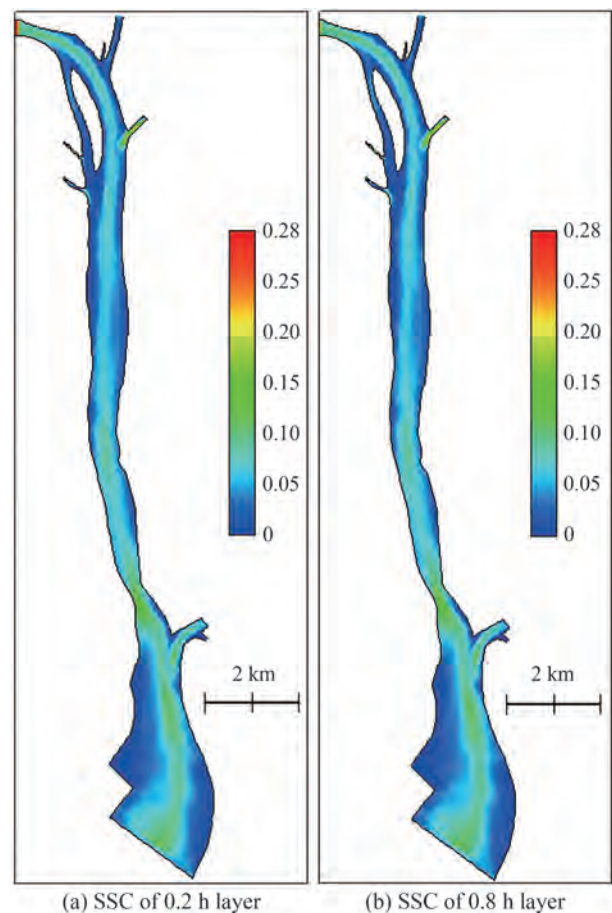
Figure 7   SSC during the ebb maximum (kg /m^3)

deserves further investigation: why does the abnormally high surface velocity have almost no impact on SSC?

In Figure 8d, the dissipations scarcely change corresponding to the tidal velocity similar to turbulent kinetic energy and turbulent viscosity. At high water levels, the dissipation is the smallest, while the largest value is at maximum flood tide. The turbulent dissipation at maximum ebb tide and low water level fall in between. We speculate that this temporal variation is due to the local instantaneous water depth, which may restrict the development of turbulence, and ultimately determine the turbulent dissipation ($\frac{k^{1/2}}{l}$) together with the tidal velocity. At high water levels, due to small velocity and large water depth, the turbulent dissipation is significantly weak. At maximum flood tide, the flow velocity is large, and the water level is close to the mean tide level; therefore, the turbulent dissipation maintains large.

Due to the re-suspension and increased sediment-carrying capacity, SSC is the largest at maximum flood tide. At high water levels, in pace with the decrease of velocity, the sediment gradually settles and the SSC decreases. Settling/scour lag is an interesting issue calling for special attention. As an agent, the sediment response time can be ex-
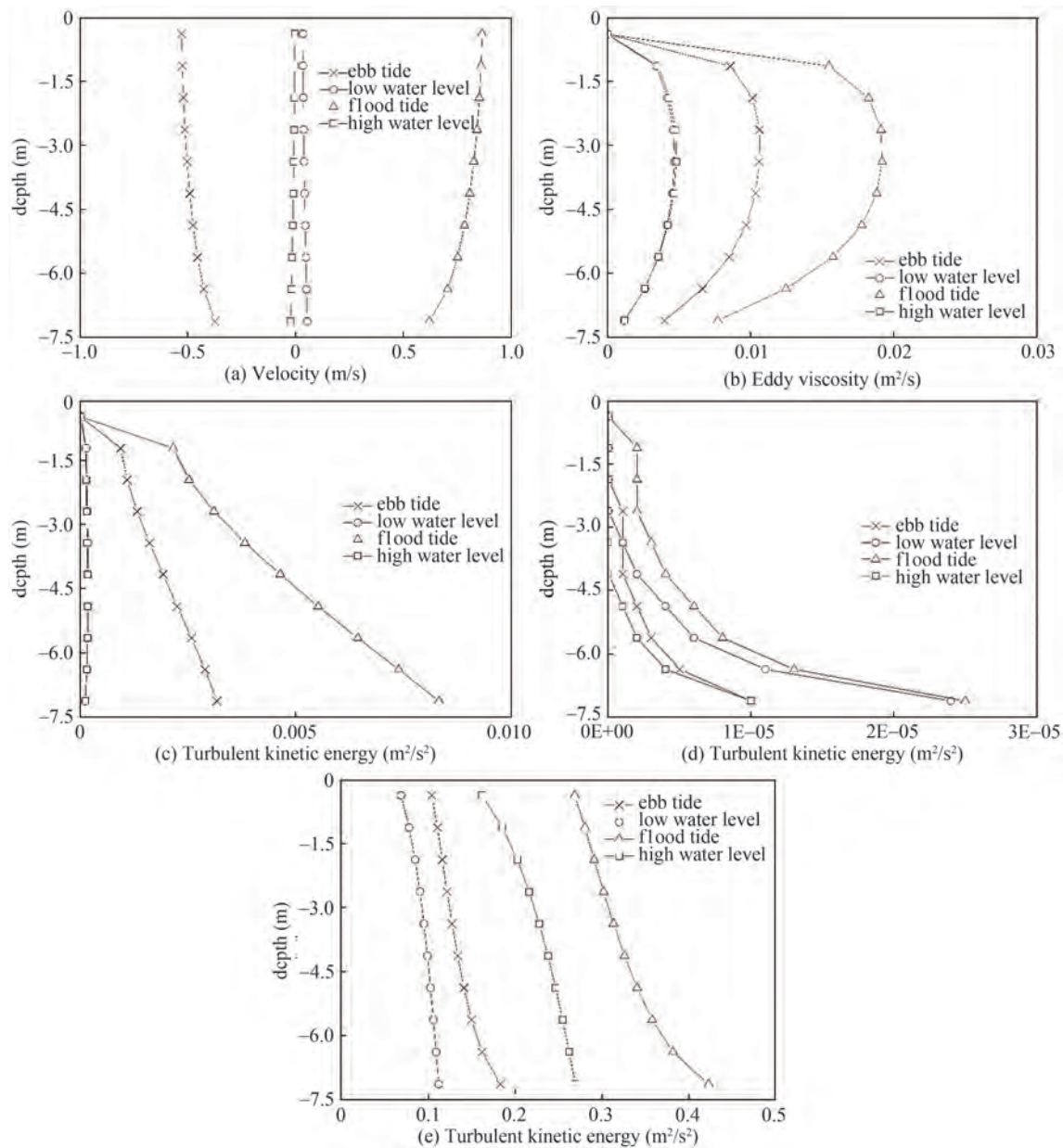
Figure 8 The vertical distribution of the simulated results during a tidal cycle at the A3

pected to be approximately equal to the vertical distance which scales the fall off sediment concentration divided by the suspended sediment fall velocity (Friedrichs et al., 1998). Analogously, the sediment response time is about 20 min in the Yamen Channel. Therefore, it can be prudently considered that the lag effect is not significant. After the high water levels, the sediment keeps settling. The maximum ebb velocity is generally less than 0.5 ms^{-1}, which is not strong enough for sediment incipience corresponding to a median particle size of 0.05 mm. Therefore, during the whole ebb period, the SSC would not increase. This process can also be seen in Figure 5, where the period of SSC is about semi-diurnal rather than quarter-diurnal. Although the turbulent viscosity is the greatest at maxi-

mum flood tide (Figure 8d), a certain vertical gradient of SSC still exists due to the resuspension from the seabed acting as a sediment source. At high water levels, the vertical distribution of SSC is more uniform than that at maximum flood tide. Since the weakened turbulent mixing and the sediment settling result in more suspended sediment loss in the upper layer than in the lower layer, the SSC in the surface layer is slightly smaller consequently. At maximum ebb tide, although the suspended sediment cannot be supplemented by the resuspension, the SSC is uniform in the vertical due to the enhanced turbulent mixing. At the low water level, the SSC is extremely low, and the vertical variation is insignificant.

5 Conclusions

Based on the coupled Sed-FVCOM system with two kinds of turbulence closure schemes with different stability functions implemented in the General Ocean Turbulence Model (GOTM), we carried out numerical experiments to examine the effects of turbulence parameterization on the temporal and spatial distribution of suspended sediment in a natural tidal channel.

The $k–kl$ scheme with three typical stability functions produces anomalously high surface currents. It can be attributed to the improper wall functions embedded in the original MY2.5 closure scheme, which produces an incorrect length scale and underestimation of the turbulent viscosity near the surface. One should use the original MY2.5 with caution and select the proper wall function. The effects of each stability function on vertical dissipation are extremely small. By contrast, the $k–kl$ and $k–\varepsilon$ can produce significantly different turbulent viscosity in the vertical, and thus turbulent diffusivity. We concluded that under specified boundary and initial conditions, $k–\varepsilon$ turbulence schemes generally produce more intensive vertical mixing than the $k–kl$ does.

Allowing for the simultaneous depositional process during erosion near the water-sediment interface, we applied $k–\varepsilon$ with CB stability function in the Yamen channel, one of the eight outfalls of the Pearl River. During a tidal period, the turbulent dissipation show highly similar trends while the patterns of the SSCs differ significantly. Although velocity, turbulent viscosity, and TKE keep similar trends and magnitudes respectively, the SSCs show different patterns between low and high water due to complex mechanisms.

This paper illuminates the influence of two kinds of turbulent closure schemes with several different wall functions on velocity and SSCs in the Yamen channel, which is important to the Guangdong-Hong Kong-Marco Greater Bay Area. Our findings provide insights into, and references for, turbulent and sediment parameterization for researchers and estuarine management.

Competing interest The authors have no competing interests to declare that are relevant to the content of this article.

References

Blumberg AF, Galperin B, O'Connor DJ (1992) Modeling vertical structure of open-channel flows. Journal of Hydraulic Engineering, 118(H8), 1119-1134. https://doi.org/10.1061/(ASCE)0733-9429 (1992)118: 8(1119)

Burchard H, Baumert H (1995) On the performance of a mixed-layer model based on the $k–\varepsilon$ turbulence closure. Journal of Geophysical Research 100, 8523-8540. https://doi.org/10.1029/94JC03229

Burchard H, Bolding K (2001) Comparative analysis of four second-moment turbulence closure models for the oceanic mixed layer. Journal of Physical Oceanography, 31, 1943-1968. https://doi.org/10.1175/1520-0485(2001)031<1943:CAOFSM>2.0.CO; 2

Burchard H, Craig PD, Gemmrich JR, van Haren H, Mathieu PP, Meier HEM, Smith WAMN, Prandke H, Rippeth TP, Skyllingstad ED, Smyth WD, Welsh DJS, Wijesekera HW (2008) Observational and numerical modelling methods for quantifying coastal ocean turbulence and mixing. Progress in Oceanography 76, 399-442. https://doi.org/10.1016/j.pocean.2007.09.005

Burchard H, Gräwe U, Holtermann P, Klingbeil K, Umlauf L (2014) Turbulence Closure Modelling in Coastal Waters. Die Küste 81, 69-87

Burchard H, Petersen O, Rippeth T (1998) Comparing the performance of the Mellor-Yamada and the $k–\varepsilon$ two-equation turbulence models. Journal of Geophysical Research, 103, 10543-10554. https://doi.org/10.1029/98JC00261

Canuto VM, Howard A, Cheng Y, Dubovikov MS (2001) Ocean turbulence. Part I: one-point closure model-momentum and heat vertical diffusivities. Journal of Physical Oceanography 31, 1413-1426. https://doi.org/10.1175/1520-0485(2001)031<1413:OTPIOP>2.0.CO;2

Chen C, Beardsley RC (1998) Tidal mixing and cross-frontal particle exchange over a finite amplitude asymmetric bank: a model study with application of Georges Bank. Journal of Marine Research 56, 1163-1201. https://doi.org/10.1357/002224098765093607

Chen X, Chen Y, Lai G (2003) Modeling of the transport of suspended solids in the estuary of Zhujiang River. Acta Oceanological Sinica, 25(2), 120-127. https://doi.org/10.1353/crt.2004.0011

Chen C, Huang H, Beardsley RC, Liu H, Xu Q, Cowles G (2007) A finite-volume numerical approach for coastal ocean circulation studies: comparisons with finite difference models. Journal of Geophysical Research, 112, https://doi.org/10.1029/2006JC003485

Choi Y, Park Y, Choi M, Jung KT, Kim KO (2021) A fine grid tide-wave-ocean circulation coupled model for the Yellow Sea: comparison of turbulence closure schemes in reproducing temperature distributions. Journal of Marine Science and Engineering 9(21): 1460. https://doi.org/10.3390/jmse9121460

Costa A, Doglioli AM, Marsaleix P, Petrenko AA (2017) Comparison of in situ microstructure measurements to different turbulence closure schemes in a 3-D numerical ocean circulation model. Ocean Modelling 120: 1-17. https://doi.org/10.1016/j.ocemod.2017.10.002

Ding Y, Chen C, Beardsley RC, Bao X, Shi M, Zhang Y, Lai Z, Li R, Lin H, Viet NT (2013) Observational and model studies of the circulation in the Gulf of Tonkin, South China Sea. Journal of Geophysical Research: Oceans 118, 6495-6510. https://doi.org/10.1002/2013JC009455

Egbert GD, Erofeeva SY (2002) Efficient inverse modeling of barotropic ocean tides. Journal of Atmospheric and Oceanic Technology 19(2), 183-204, 2002. https://doi.org/10.1175/1520-0426(2002)019<0183:EIMOBO>2.0.CO;2

Friedrichs CT, Armbrust BD, Swart HED (1998) Hydrodynamics and equilibrium sediment dynamics of shallow, funnel-shaped tidal estuaries. Physics of Estuaries and Coastal Seas, Dronkers & Scheffers (Eds). Balkema, Rotterdam, 315-327

Galperin B, Kantha LH, Hassid S, Rosati A (1988) A quasi-equilibrium turbulent energy model for geophysical flows. Journal of the Atmospheric Sciences 45(1), 55-62. https://doi.org/10.1175/1520-0469(1988)045<0055:AQETEM>2.0.CO;2

Geyer WR, Ralston DK (2015) Estuarine frontogenesis. Journal of Physical Oceanography, 45(2): 546-561. https://doi.org/10.1175/

JPO-D-14-0082.1

Gong W, Zhang H, Schuttelaars HM (2016) Tidal asymmetry in a funnel-shaped estuary with mixed semidiurnal tides. Ocean Dynamics 66: 637-658. https://doi.org/10.1007/s10236-016-0943-1

Hansen DV, Rattray M (1965) Gravitational Circulation in Straits and Estuaries. Journal of Marine Research 23(2): 104-122. https://doi.org/10.1357/002224021834614399

Kantha LH, Clayson CA (1994) An improved mixed layer model for geophysical applications. Journal of Geophysical Research, 99, 25235-25266. https://doi.org//10.1029/94JC02257

Lai Z, Ma R, Gao G, Chen C, Beardsley RC (2015) Impact of multichannel river network on the plume dynamics in the Pearl River estuary. Journal of Geophysical Research: Oceans, 120(8), 5766-5789. https://doi.org/10.1002/2014JC010490

Li R, Luo F, Zhu W (2008) The suspended sediment transport equation and its near-bed sediment flux. Science in China Series E: Technological Sciences, 52: 387-391. https://doi.org/10.1007/s11431-008-0175-9

Li M, Zhong L, Boicourt WC (2005) Simulations of Chesapeake Bay estuary: Sensitivity to turbulence mixing parameterizations and comparison with observations. Journal of Geophysical Research Oceans 110(12): 347-356. https://doi.org/10.1029/2004JC002585

Lima HP, Dias FJS, Teixeira C, Godoi VA, Torres Jr. AR, Araujo RS (2021) Implications of turbulence in a macrotidal estuary in northeastern Brazil-The São Marcos Estuarine Complex. Regional Studies in Marine Science, 47. https://doi.org/10.1016/j.rsma.2021.101947

Liu J, Yuan J, Liang J (2022) An evaluation of vertical mixing parameterization of ocean boundary layer turbulence for cohesive sediments, Deep Sea Research Part II: Topical Studies in Oceanography 204. https://doi.org/10.1016/j.dsr2.2022.105168

Ralston DK, Cowles GW, Geyer WR, Holleman RC (2017) Turbulent and numerical mixing in a salt wedge estuary: dependence on grid resolution, bottom roughness, and turbulence closure. Journal of Geophysical Research: Ocean 122: 692-712. https://doi.org/10.1002/2016JC011738

Reffray G, Bourdallé-Badie R (2015) Modelling turbulent vertical mixing sensitivity using a 1-D version of NEMO. Geoscientific Model Development, 8: 69-86. DOI: 10.5194/gmd-8-69-2015

Reissmann J, Burchard H, Feistel R, Hagen E, Lass H, Volker, Mohrholz, Nausch G, Umlauf L, Wieczorek G (2009) State-of-the-art review on vertical mixing in the Baltic Sea and consequences for eutrophication. Progress in Oceanography, 82: 47-80. https://doi.org/10.1016/j.pocean.2007.10.004

Rodi W (1984) Turbulence models and their application in hydraulics. A state of the art review. United States: N. P., Web

Song D, Wang XH, Kiss AE, Bao X (2011) The contribution to tidal asymmetry by different combination of tidal constituents. Journal of Geophysical Research, 116: 1-12. https://doi.org/10.1029/2011JC007270

Sun Y, Chen C, Beardsley RC, Ullman D, Butman B, Lin H (2016) Surface circulation in Block Island Sound and adjacent coastal and shelf regions: A FVCOM-CODAR comparison. Progress in Oceanography, 143: 26-45. https://doi.org/10.1016/j.pocean.2016.02.005

Tu J, Fan D, Zhang Y, Voulgaris G (2019) Turbulence, sediment-induced stratification, and mixing under macrotidal estuarine conditions (Qiantang Estuary, China). Journal of Geophysical Research: Oceans, 124, 4058-4077. https://doi.org/10.1029/2018JC014281

Umlauf L, Burchard H (2011) Diapycnal transport and mixing efficiency in stratified boundary layers near sloping topography. Jouranl of physical oceanography, 41, 329-345. https://doi.org/10.1175/2010JPO4438.1

Umlauf L, Burchard H, Bolding K (2003) Extending the $k - \omega$ turbulence model towards oceanic applications. Ocean Modeling, 5, 195-218. https://doi.org/10.1016/S1463-5003(02)00039-2

Van Rijn (2005) Principles of sedimentation and erosion engineering in rivers, estuaries and coastal seas. AQUA Publications

Warner JC, Sherwood CR, Arango HG, Signell RP (2005) Performance of four turbulence closure models implemented using a generic length scale method. Ocean Modelling, 8(1-2): 81-113. https://doi.org/10.1016/j.ocemod.2003.12.003

Warner JC, Sherwood CR, Signell RP, Harris CK, Arango HG (2008) Development of a three-dimensional, regional, coupled wave, current, and sediment-transport model. Computers & Geoscience 34: 1284-1306. https://doi.org/10.1016/j.cageo.2008.02.012

Willmott CJ (1981) On the Validation of Models. Physical Geography, 2: 184-194. https://doi.org/10.1080/02723646.1981.10642213

Wu H, Wang Y, Gao S, Xing F, Tang J, Chen D (2022) Fluid mud dynamics in a tide-dominated estuary: A case study from the Yangtze River. Continental Shelf Research 232, https://doi.org/10.1016/j.csr.2021.104623

Yang X, Wang W (1994) A statistical study on hydrodynamic sedimentation and sand movement Huangmaohai Estuary Bay (in Chinese). The Ocean Engineering, 12(4): 45-51

Yang Y, Guan W, Deleersnijder E, He Z (2022) Hydrodynamic and sediment transport modelling in the Pearl River Estuary and adjacent Chinese coastal zone during Typhoon Mangkhut. Continental Shelf Research 233. https://doi.org/10.1016/j.csr.2022.104645

Zhang G, Cheng W, Chen L, Zhang H, Gong W (2019) Transport of riverine sediment from different outlets in the Pearl River Estuary during the wet season. Marine Geology, 415, https://doi.org/10.1016/j.margeo.2019.06.002